Significance of Microtearing Turbulence in Turbulence-Reduced High-Density-Gradient Plasmas in Wendelstein 7-X

H. Cu-Castillo,[1,*] A. Bañón Navarro,[1] G. Merlo,[1] F. Reimold,[2] T. Romba,[2] O. Ford,[2] S. Bannmann,[2] L. Vanó,[2] M. Wappl,[2] J. Geiger,[2] A. Goodman,[2] A. Zocco,[2] F. Jenko,[1] and W7-X Team[†]

[1]*Max-Planck-Institut für Plasmaphysik, Boltzmannstraße 2, 85748 Garching, Germany*
[2]*Max-Planck-Institut für Plasmaphysik, Wendelsteinstraße 1, 17489 Greifswald, Germany*

(Received 20 October 2025; revised 20 February 2026; accepted 21 April 2026; published 14 July 2026)

Gyrokinetic simulations of a turbulence-reduced Wendelstein 7-X discharge—characterized by a steep density gradient, moderate temperature gradients, and low plasma beta—show that microtearing mode (MTM) turbulence dominates transport. The simulated heat and particle fluxes agree with experimental measurements, leaving MTMs as the only mode consistent with the data. These conditions, the quasi-isodynamic and nearly max-J magnetic configuration of the Wendelstein 7-X stabilize ion temperature gradient modes and density-gradient-driven trapped-electron modes, while moderate collisionality and low magnetic shear further enable MTM growth. Further nonlinear scans of the density gradient reveal a significant reduction in turbulent transport at the experimentally observed threshold, which we identify as an ion temperature gradient to MTM-dominated turbulence transition. These findings provide a robust explanation for the turbulence suppression and deepen our understanding of low turbulent transport regimes in optimized stellarators.

DOI: 10.1103/nd3p-yb9t

The Wendelstein 7-X (W7-X) is the world's most advanced stellarator and aims to demonstrate that its magnetic confinement concept is a viable path toward a fusion power plant. Recently, the W7-X has achieved record-breaking discharges with performance levels on par with leading tokamaks [2], and its improved confinement can be sustained over long durations [3]. This success is largely attributed to its optimized magnetic configuration, designed to minimize neoclassical transport losses, among other criteria [4]. As in tokamaks, however, plasma confinement in the W7-X is ultimately limited by microturbulence [5–9].

Low turbulent transport W7-X scenarios are characterized by steep density gradients (∇n), which can be driven by core fueling techniques such as frozen hydrogen pellet injection [10] or neutral beam injection (NBI) [11]. Under these conditions, the plasma exhibits reduced turbulent heat transport [10–12] and favorable confinement of particles (hydrogen ions and electrons) [13], but it may also suffer from impurity accumulation [14,15]. Understanding the nature of turbulence in these regimes is therefore crucial to achieve a balance between improved energy and particle confinement and the expulsion of impurities.

This Letter demonstrates that microtearing mode (MTM) turbulence not only dominates in a W7-X discharge with low turbulent transport and high ∇n, but it also constitutes the residual turbulence once the more deleterious ion temperature gradient (ITG) mode is suppressed. MTMs are small-scale electromagnetic instabilities that cause tearing and reconnection of magnetic field lines. They are driven by the electron temperature gradient and are influenced by magnetic shear, a measure of magnetic field line bending [16,17]. In slab geometry (i.e., in a homogeneous magnetic field), they are caused by an imbalance in the force balance parallel to the magnetic field due to a time-dependent electron thermal force, and collisions can be crucial for their destabilization [18,19]. MTM turbulence has been previously identified as relevant in several tokamak experiments [20–22]. By simulating microturbulence with the gyrokinetic code GENE [23], we (i) identify MTM turbulence as the only candidate able to reproduce the experimentally measured heat and particle fluxes, and (ii) show that once the detrimental ITG turbulence is stabilized by a large ∇n, the benign MTM turbulence takes over transport, hence solving the long-standing question of turbulence suppression in an optimized stellarator.

[*]Contact author: hugo.cu.castillo@ipp.mpg.de
[†]See Supplemental Material [1] for the W7-X Team.

Experimental scenario and numerical setup—The case studied is the NBI-heated phase of the high mirror configuration discharge No. 20181009.034 in the W7-X. After an initial start-up with electron cyclotron resonance heating (ECRH) and neutral gas fueling, both systems are turned off once the plasma density is sufficient. Then, the NBI injected fuel and provided a total heating of $P \approx 2.6$ MW over a broad plasma volume. During this interval, the central density and its gradient increase while the electron and ion temperatures remain constant and roughly equal to each other [11,13]. Low turbulent transport in high-density-gradient plasmas is manifested experimentally by a reduced heat diffusivity, χ, at mid radius (defined by $Q_{\text{tot}} = 2n\chi\nabla T$). In the present NBI-heated discharge χ is 4 times smaller than in ECRH plasmas that exhibit larger turbulence and small density gradients [11]. The low heating per particle in this NBI-heated phase makes that $f_{\text{ren}} = \tau_E/\tau_{\text{ISS04}} = 0.7$ (with τ_E the energy confinement time and τ_{ISS04} the ISS04 scaling [24]). ECRH plasmas typically have $f_{\text{ren}} \approx 0.6$ [12,25].

The time analyzed is $t = 2.8$ s and unless stated otherwise, the radial location is $\rho \equiv r_{\text{eff}}/a = 0.4$. The effective radius is defined as $r_{\text{eff}} = \sqrt{A/\pi}$, where A is the area enclosing the selected flux surface and $a = 0.52$ m is the plasma minor radius. The numerical plasma parameters used to represent the experiment at this position are $a/L_{n_e} = 2.37$, $a/L_{T_e} = 1.54$, $a/L_{T_i} = 1.91$, $T_i = 1.1T_e$, $\beta_e = 8\pi n_e T_e/B_{\text{ref}}^2 = 5.2 \times 10^{-3}$ (in CGS units), and normalized collision frequency [26] $\nu_c = \pi \ln \Lambda q_e^4 n_e a/(2^{3/2}T_e^2) = 2.21 \times 10^{-3}$. Here, $a/L_\xi = -a/\xi(d\xi/d\rho)$ denotes the normalized scale length of a given quantity ξ, B_{ref} is the reference magnetic field strength and the subscripts (e, i) refer to the corresponding electron and main ion quantities. The magnetic shear at this radial position is $\hat{s} = \rho_0/q_0(dq/d\rho) = -0.021$, where $q = 1/\iota$ is the safety factor (with ι being the rotational transform), and ρ_0 and $q_0 = -1.14$ are the reference radial position and safety factor, respectively.

Simulations were performed using the local version of the gyrokinetic code GENE, which evolves small-scale plasma fluctuations while incorporating electromagnetic effects and collisions. The latter are modeled using the linearized Landau-Boltzmann operator. The simulation coordinates are aligned to the background magnetic field, $\mathbf{B}_0 = \nabla x \times \nabla y$, where $x = \rho$ is the radial coordinate, and y is the binormal coordinate given by $y = x_0/q_0(q_0\theta^* - \phi)$, with $\theta^* = z$ the PEST poloidal angle [27] and ϕ the toroidal angle. The velocity space of the perturbed distribution function δf is discretized in terms of the velocity parallel to the magnetic field line $v_\parallel$ and the magnetic moment $\mu = m_i v_\perp^2/(2B_0)$.

We performed both linear and nonlinear simulations. Unless stated otherwise, for the linear runs, the numerical resolution was $(n_x, n_{k_y}, n_z) = (48, 1, 192)$ in the spatial directions, and $(n_{v_\parallel}, n_\mu) = (32, 12)$ in velocity space. The simulation domain in velocity space was $(\pm l_{v_\parallel}, l_\mu) = (\pm 3\sqrt{2}c_s, 9T_e/B_0)$, where $c_s = \sqrt{T_e/m_i}$ is the reference speed. The standard twist-and-shift boundary condition [28] was applied after two poloidal turns ("npol"), unless otherwise specified, in which case the generalized boundary condition of Ref. [29] was used. Nonlinear simulations employed a resolution of $(n_x, n_{k_y}, n_z, n_{v_\parallel}, n_\mu) = (288, 36, 768, 32, 24)$. The simulation domain sizes were $(l_x, l_y) = (288\rho_s, 314.15\rho_s)$, and eight poloidal turns. This study excludes impurity effects as their contribution has a negligible impact on the linear growth rates γ, as indicated in Fig. 1(a). Experimentally, the impurity presence was characterized by $a/L_{n_{C^{6+}}} = 2.3$ and $n_{C^{6+}} = 3 \times 10^{-3} n_e$. Parallel magnetic field fluctuations were also excluded as they had no effect on the growth rate (not shown), and it was corroborated that the kinetic ballooning mode was still stable [9].

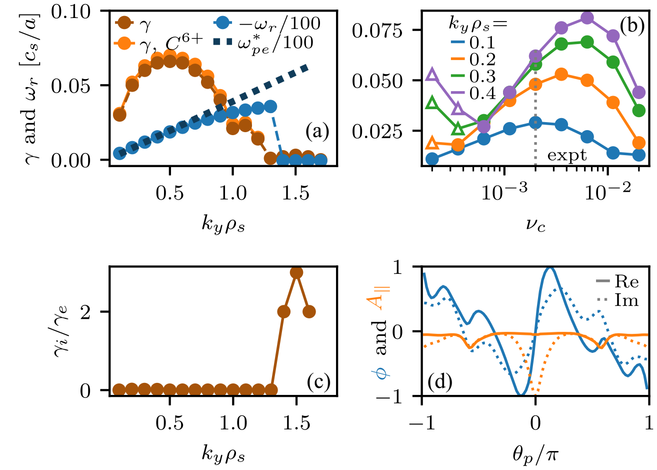

FIG. 1. Linear gyrokinetic characterization of instabilities. (a) Growth rate and real frequency as a function of $k_y\rho_s$. Impurity contribution (orange) is negligible. The dotted line indicates the electron diamagnetic frequency $\omega_{p_e}^*$. (b) Growth rate versus normalized collision frequency for various $k_y\rho_s$. The experimental collisionality is marked by a vertical dashed line. Full circles denote MTMs; hollow triangles denote a trapped-particle mode (TPM). The changes for $k_y\rho_s = 0.1$ were $(n_x, n_z) = (64, 288)$ and 3 npol. (c) Ratio of the contributions to the growth rate from ions and electrons. (d) Tearing parity at $k_y\rho_s = 0.5$: odd parity in ϕ (blue) and even in $A_\parallel$ (orange), normalized to their respective maxima. Only the central ballooning angle region is shown.

Mode identification—We performed a linear gyrokinetic stability analysis under the experimental conditions described above. The results, summarized in Fig. 1, indicate that the dominant instability over a broad range of binormal wave numbers ($0.1 \le k_y\rho_s \le 1.4$) is the microtearing mode. This is characterized by a negative real frequency $\omega_r < 0$, indicating propagation in the electron diamagnetic direction, as shown in Fig. 1(a). The reference gyroradius is $\rho_s = c_s/\Omega_{\rm ref}$, and $\Omega_{\rm ref} = q_e B_{\rm ref}/(m_i c)$ is the reference gyrofrequency (in CGS units). Moreover, the real frequency closely follows the electron diamagnetic drift frequency, $\omega_r \approx \omega^*_{p_e} = k_y\rho_s c_s(1/L_{T_e} + 1/L_n)$, consistent with the slab semicollisional MTM regime predicted by analytical theory [16,17].

Additional features reinforce the identification of the linearly dominant mode as an MTM. The parity structure of the eigenmodes [Fig. 1(d)] has odd parity in the electrostatic potential ϕ and even parity in the parallel vector potential $A_\parallel$, as expected for tearing modes. The species-resolved contributions to the growth rate [30], shown in Fig. 1(c), shows a clear dominance of the electron response. Furthermore, the growth rate dependence on collisionality in Fig. 1(b) exhibits a nonmonotonic trend, a characteristic trend of MTMs [16]. At lower collisionalities, a trapped-particle mode (TPM) emerges, characterized by its electrostatic nature with ballooning parity, $\omega_r \lesssim 0$, driven by ∇n, and heat flux localization at magnetic wells (not shown), and is similar to what was referred to in Ref. [31] as the ion-driven trapped-electron mode (iTEM). Because $\gamma_i/\gamma_e \gtrsim 1$ for this case, it is unlikely to be the collisionless trapped-electron mode (TEM) [32].

Linear parametric scan—The presence of the MTM instability in this NBI-heated plasma can be attributed to a combination of destabilizing and stabilizing mechanisms. According to slab semicollisional theory, MTMs are driven by the electron temperature gradient a/L_{Te} and are influenced by the magnetic shear $\hat{s}$ [16,17]. Although the W7-X has a much more complex geometry than the slab model, we find that the qualitative behavior of MTMs remains consistent with these theoretical predictions. Figure 2(a) confirms that the MTM growth rate increases with the electron temperature gradient. For the W7-X, decreasing $|\hat{s}|$ enhances the MTM growth rate [Fig. 2(b)]. To execute this scan, the magnetohydrodynamic equilibrium was modified self-consistently by introducing localized artificial currents near $\rho = 0.4$; this altered $\hat{s}$ while leaving the remaining geometric quantities essentially unchanged. Earlier work [16,33] showed that the MTM growth rate dependence on $\hat{s}$ is generally nonmonotonic: at modest shear an increase of $\hat{s}$ is destabilizing, whereas at very low shear the same increase becomes stabilizing [21,33,34]. The trend observed in Fig. 2(b) is consistent with the latter regime. A theoretical explanation of the shear dependence in this regime is left for the future.

To test the robustness of MTMs within experimental error bars, we performed scans of the ion temperature gradient a/L_{T_i} and the density gradient a/L_n. Figure 2(c) shows that a/L_{T_i} has a negligible effect on MTMs except when $\eta_i = L_n/L_{T_i} \gtrsim 1.7$—about twice the experimental value $\eta_{i,\rm expt} = 0.8$, where ITGs become unstable. The density gradient a/L_n has a minimal impact on MTMs [Fig. 2(d)] and even slightly stabilizes them as a/L_n increases. Unlike tokamaks, the simulations indicate a

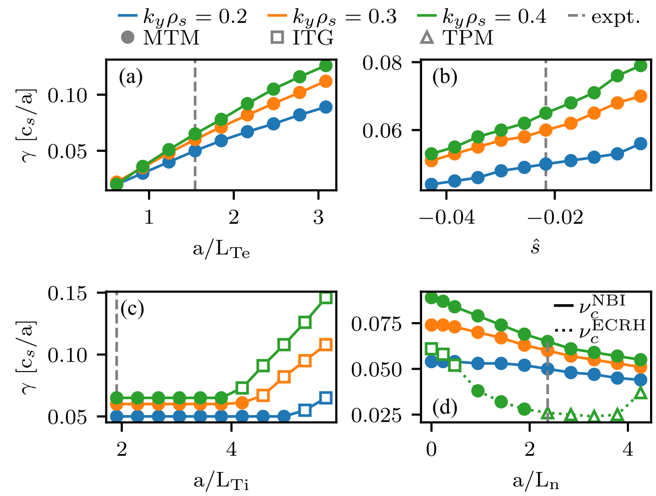

FIG. 2. Dependence of MTM growth rate on (a) electron temperature gradient, (b) global magnetic shear, (c) ion temperature gradient, and (d) density gradient. The nominal NBI collisionality (solid line) and the reduced collisionality of the ECRH reference case mentioned in the text were used (dotted line). Vertical dashed lines indicate experimental values.

strong resilience against the deleterious collisionless ∇n-driven TEM as a result of the quasi-isodynamic (QI) geometry of the W7-X, its nearly max-J property, and the low experimental η_e and η_i [35]. Interestingly, MTMs remain unstable even at low a/L_n, and this contrasts with a subset of ECRH plasmas with flat density profiles where the ITG is expected to prevail [25]. To examine this discrepancy, we used as reference the ECRH discharge No. 20180920.017, which exhibits characteristics of ITG dominance both in the experiment and in flux-matched gyrokinetic simulations [8,36]. At $\rho = 0.4$, its normalized collision frequency $\nu_c = 5.6 \times 10^{-4}$ ($n_e \approx 6 \times 10^{19}$ m^{-3} and $T_e \approx 1.4$ keV) is roughly one fourth of the normalized collision frequency of the NBI-heated discharge analyzed ($\nu_c = 2.2 \times 10^{-3}$, with $n_e = 7.9 \times 10^{19}$ m^{-3} and $T_e =$ 0.79 keV). This is an important parameter as a very low value of collisionality can stabilize MTMs [Fig. 1(d)]. Indeed, repeating the linear scan with this ECRH-ν_c, ITG modes appear at flat density profiles, MTMs appear at moderate a/L_n and the TPMs described earlier become dominant at high a/L_n, as shown by the dashed line in Fig. 2(d).

These observations lead to two qualitative conclusions. First, MTMs are mostly insensitive to density gradient, confirming that they are primarily driven by electron temperature gradient. Second, the numerical transition observed from ITG dominance in the reference ECRH case to MTM dominance in the NBI case cannot be explained by the change in density gradient alone, but it also needs to consider the magnitude of the collisionality.

Having identified the parameters that control MTMs, we investigated the radial region over which they remain active. MTM activity is not localized and remains unstable

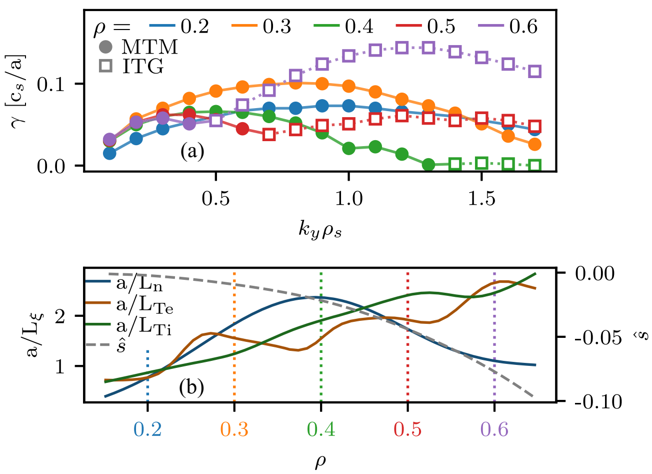

FIG. 3. (a) Growth rates and unstable modes as a function of $k_y\rho_s$ at different radial positions. MTMs are indicated by circles and solid lines, while ITGs by hollow squares and dotted lines. (b) Normalized gradient scale lengths and magnetic shear $\hat{s}$ versus radius. The color of the vertical dotted lines indicate the radial positions of the linear simulations in (a).

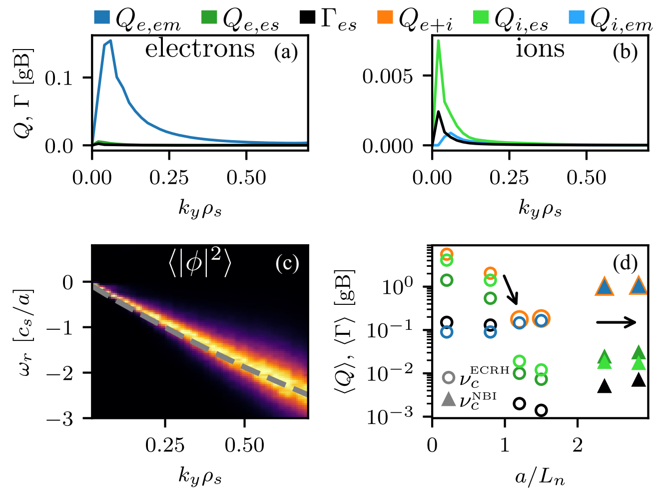

FIG. 4. Particle flux, electrostatic (es) and electromagnetic (em) heat flux spectra of (a) electrons and (b) ions in gyro-Bohm units, $[\Gamma] = n_e c_s (\rho_s/a)^2$ and $[Q] = n_e T_e c_s (\rho_s/a)^2$. (c) Frequency spectrum of electrostatic potential as a function of $k_y\rho_s$; the dashed line indicates the real frequency obtained in linear simulations [Fig. 1(a)]. (d) Flux-surface-averaged heat and particle fluxes as a function of a/L_n. Results are shown for the collisionality of the experimental NBI case ν_c^{NBI} (solid triangles) and for the reference ECRH plasma ν_c^{ECRH} (hollow circles). Orange markers depict the sum of electron and ion heat fluxes. Ion electromagnetic heat flux is not shown.

throughout the radial interval $0.2 \le \rho \le 0.6$, as illustrated in Fig. 3(a), which shows linear simulations using the corresponding experimental parameters at the selected radii. MTMs are facilitated by the low magnetic shear $\hat{s}$ in the inner plasma, which mitigates MTM damping and the sufficiently large density gradients that stabilize ITG modes, as shown in Fig. 3(b).

Microtearing mode turbulence—Nonlinear gyrokinetic simulations using the full set of experimental parameters for $\rho = 0.4$ yield turbulent fluxes in good agreement with the measured ones: the simulated heat and particle fluxes are $A\langle Q\rangle_{\mathrm{sim}} = 0.84 \pm 0.02$ MW and $A\langle\Gamma\rangle_{\mathrm{sim}} = 4.3 \pm 0.03 \times 10^{19}\ \mathrm{s}^{-1}$, compared to the experimental estimates of $A\langle Q\rangle_{\mathrm{expt}} = 0.6$ MW and $A\langle\Gamma\rangle_{\mathrm{expt}} = 9.9 \pm 4.4 \times 10^{19}\ \mathrm{s}^{-1}$ (see Figs. 8 and 12 of Ref. [11]). Here, $\langle\cdot\rangle$ indicates a flux surface and time average.

The heat and particle flux spectra are shown in Figs. 4(a) and 4(b) (the total fluxes correspond to the sum of their respective spectral components at all wave numbers $k_y\rho_s$ [37]). Electron electromagnetic heat flux dominates over the electrostatic contributions—a well-established signature of MTM turbulence [38]. ITG turbulence is absent due to a combination of the low η_i and moderate ν_c, consistent with the linear scans in Figs. 2(c) and 2(d). Turbulence generated by the electron temperature gradient mode is considered negligible as this mode is stable in linear simulations (not shown), in line with the low $\eta_e = 0.65$. Both branches of the TEM—those driven by ∇T_e and ∇n—are absent. The background $E \times B$ shear has minimal impact on the time-averaged electromagnetic flux, with $\hat{\gamma}_{E\times B} = 0.037$ $[c_s/a]$ (not shown), consistent with standard tokamak simulations where MTM growth rates are comparable to the shearing rate [21,39].

While MTMs typically generate negligible particle transport in tokamaks [39], in this particular case they appear to drive all the particle flux, which is mostly electrostatic. This can be observed in the frequency spectrum [Fig. 4(b)], where the electrostatic potential matches the MTM frequencies identified in linear simulations [Fig. 1(a)], and no other dominant or subdominant modes at relevant wave numbers for the particle flux are found.

Compatibility with W7-X experiments—MTM turbulence is characterized by $Q_e \gg Q_i$. This situation is experimentally plausible in NBI-heated plasmas because, as explained in Ref. [11], it is within the limits of diagnostic uncertainty that the turbulent ion heat flux Q_i is zero at the analyzed radius of this NBI-heated plasma.

Two other experimental observations support the existence of MTM turbulence in high-density-gradient regimes. First, in discharges with $a/L_n > 1$, the ion heat flux channel is small and the electron contribution dominates [12], also seen in high performance scenarios requiring a large a/L_n [10]. Second, the total turbulent heat flux for discharges with $a/L_n > 1$ (including this one), is low compared to cases with $a/L_n < 1$ and is not exacerbated by the density gradient [11,12], suggesting that the main driving instability is insensitive to a/L_n. This behavior is explained if MTMs dominate: the turbulent heat flux is primarily carried by electrons ($Q_{\mathrm{tot}} \approx Q_e$), and is unaffected by the density gradient. This is evident from the triangle markers in Fig. 4, where all the nominal parameters were held fixed and a 20% increase in a/L_n did not affect the heat flux substantially. A similar behavior has been observed in MTMs in tokamak pedestals (Fig. 17 of Ref. [38]). The decoupling between Q_{tot} and a/L_n for MTMs is in stark contrast to density-gradient-driven modes such as the ∇n-driven TEM branch, and the previously proposed iTEM and universal instability (UI) in electrostatic and/or collisionless conditions [40–44]. This reflects the fact that MTMs are primarily driven by the electron temperature gradient.

To further exclude the presence of the iTEM and the UI in this case, we performed nonlinear simulations keeping all physical parameters fixed except for ν_c, set to zero, and β_e, reduced to 10^{-5}. In these limits, the TPMs resembling the iTEM and the UI modes became dominant, respectively. The numerical parameters for the collisionless and the electrostatic cases had the grid resolution and box sizes $(n_x, n_{k_y}, n_z, n_{v_\parallel}, n_\mu) = \{(128, 64, 192, 32, 12); (256, 32, 384, 32, 12)\}$, $(l_x, l_y, \mathrm{npol}) = \{(128\rho_s, 157\rho_s, 2.05); (384\rho_s, 209.44\rho_s, 4)\}$, applying the generalized and twist-and-shift parallel boundary conditions, respectively. In both cases, the total turbulent flux-surface and time-averaged heat and particle fluxes were several orders of magnitude larger than those of the experiment: $A\langle Q_{\nu_c=0}\rangle = 6.7$ MW and $A\langle \Gamma_{\nu_c=0}\rangle = 1\times 10^{22}$ s^{-1} for the collisionless case, and $A\langle Q_{\beta_e=10^{-5}}\rangle = 32$ MW and $A\langle \Gamma_{\beta_e=10^{-5}}\rangle = 4.2\times 10^{22}$ s^{-1} for the electrostatic case. Collisionality suppresses the iTEM [45] [see also Fig. 1(d)], while β_e stabilizes the UI [46–48]. These results rule out iTEM and UI, leaving MTM as the only mode consistent with the measured fluxes. Furthermore, the experimentally observed negligible ion heat flux at large a/L_n is not reproduced when the UI or iTEM dominate, as seen in our simulations and in earlier works (see, e.g., Fig. 21 of Ref. [44]). The exclusion of these instabilities in high-density-gradient scenarios suggests that the current explanation of the turbulence suppression mechanism in the W7-X is incomplete. Therefore, we revisit this topic in the next section.

Turbulence suppression mechanism—The analysis of the W7-X experimental database in Ref. [12] concluded that a/L_n is the main parameter for suppressing turbulence, a tendency observed in all fueling and heating schemes. This indicates a fundamental plasma physics property rather than a consequence of any specific mode of operation of the device. Earlier modeling aimed at explaining this phenomenon either employed adiabatic electrons [40] or kinetic electrons with a nonzero a/L_{T_e} but in the electrostatic, collisionless limit [49]; these studies yielded only modest stabilization and could not be compared quantitatively with experiment. By adding the missing physics—collisionality and electromagnetic fluctuations– we demonstrated that MTM turbulence dominates transport when a/L_n is steep. We agree that increasing a/L_n stabilizes the ITG drive, but the residual transport must be carried by a mode that (i) is insensitive to a/L_n and (ii) exists under experimentally relevant conditions. To illustrate that the MTM fulfills these conditions, we performed a series of nonlinear simulations in which all physical parameters of the NBI discharge were held fixed while a/L_n was varied and the collisionality was reduced to the reference ECRH value, similarly as in Fig. 2(d). The results [Fig. 4(d), hollow circles] show a clear transition from ITG-dominated turbulence—characterized by large electrostatic heat fluxes—to MTM-dominated turbulence —featuring dominant electron electromagnetic heat flux— thereby leading to a considerably lower transport. Remarkably, this transition occurs near $a/L_n \simeq 1$, roughly where experimental scenarios indicate a drastic change in behavior [12]. Once the MTM dominates, a broader operational window becomes available, allowing higher a/L_{Ti} [Fig. 2(c)], and consequently, larger pressure gradients. Simulations at $a/L_n = 1.2$ and 1.5 used the same numerical parameters as the nominal NBI case. For $a/L_n = 0.2$ and 0.8, they were $(n_x, n_{k_y}, n_z, n_{v_\parallel}, n_\mu) = \{(256, 64, 96, 32, 12), (256, 81, 192, 32, 12)\}$, $(l_x, l_y, \mathrm{npol}) = \{(256\rho_s, 125\rho_s, 1.0527); (256\rho_s, 251\rho_s, 2.091)\}$, respectively, using the generalized parallel boundary condition.

Conclusions—This Letter reports the first observation of MTM turbulence in the Wendelstein 7-X stellarator, which dominates transport once the more deleterious ITG turbulence is suppressed. In the NBI-heated scenario studied, MTMs arise from the sufficiently large density gradient, moderate temperature gradients, QI geometry, and max-J that inhibit the appearance of ITG and TEM turbulence. The emergence of MTMs is facilitated by the moderate collisionality and the low magnetic shear of the W7-X. The simulations presented here reproduce the experimental heat and particle fluxes, with collisionality and electromagnetic effects playing a crucial role. MTM-driven turbulence yields $Q_e \gg Q_i$, a result that lies within the experimental error bars in the analyzed NBI-heated discharge. In addition, the heat flux associated with this mode is electron-dominated and is insensitive to the density gradient, in agreement with W7-X experimental observations on plasmas with $a/L_n > 1$ [12]. After excluding the instabilities proposed in previous studies in these conditions, we revisited the turbulence suppression mechanism in the W7-X. By increasing the density gradient, we confirmed ITG stabilization and showed that the benign MTM turbulence dominates, thus yielding a considerably lower overall transport, which previous studies were unable to reproduce [40,42,44,49].

Although a study of MTMs in reactor-relevant scenarios is beyond this work, a future stellarator power plant could possibly benefit from low turbulent transport driven by MTMs (compared to the ITG-driven one) as current designs feature QI geometry, low magnetic shear, max-J, and pellet injection [50,51]. The benefited region is likely located near the last closed flux surface, where the comparatively low T_e yields a sufficiently high collision frequency, enabling MTMs, while the steep density gradient produced by local pellet ablation (whose location empirically scales as $T_e^{-5/9}$ [52]) stabilizes ITG.

Acknowledgments—The authors would like to thank T. Görler, D. Told, A. Di Siena, C. Angioni, F. Sheffield, and P. Costello. The simulations were performed in the HPC Clusters Raven and Viper at the Max Planck Computing and Data Facility, and Leonardo and Pitagora from Cineca HPC. This work has been carried out within the framework of the EUROfusion Consortium, funded by the European Union via the Euratom Research and Training Programme (Grant Agreement No. 101052200—EUROfusion).

Data availability—The data that support the findings of this article are not publicly available upon publication because it is not technically feasible and/or the cost of preparing, depositing, and hosting the data would be prohibitive within the terms of this research project. The data are available from the authors upon reasonable request.

[1] See Supplemental Material at http://link.aps.org/supplemental/10.1103/nd3p-yb9t for the members of the W7-X team.
[2] S. Bannmann (The W7-X Team), Phys. Rev. E (to be published), 10.1103/q59k-8m26.
[3] S, A. Bozhenkov (The W7-X Team), Plasma Phys. Controlled Fusion **68**, 055015 (2026).
[4] C. D. Beidler *et al.* (The W7-X Team), Nature (London) **596**, 221 (2021).
[5] T. Klinger *et al.*, Nucl. Fusion **59**, 112004 (2019).
[6] T. Sunn Pedersen *et al.*, Nucl. Fusion **62**, 042022 (2022).
[7] F. Wilms, A. Bañón Navarro, T. Windisch, S. Bozhenkov, F. Warmer, G. Fuchert, O. Ford, D. Zhang, T. Stange, F. Jenko (The W7-X Team), Nucl. Fusion **64**, 096040 (2024).
[8] D. L. C. Agapito Fernando *et al.* (The W7-X Team), Phys. Plasmas **32**, 073904 (2025).
[9] F. Wilms, A. B. Navarro, G. Merlo, A. Di Siena, G. Weir, T. Windisch, S. Bozhenkov, G. Fuchert, O. Ford, D. Zhang, T. Stange, E. Pasch, T. Romba, P. Z. Pölöskei, A. Langenberg, N. Pablant, F. Jenko (The W7-X Team), Phys. Plasmas **32**, 072505 (2025).
[10] S. Bozhenkov *et al.* (The W7-X Team), Nucl. Fusion **60**, 066011 (2020).
[11] O. Ford *et al.* (The W7-X Team), Nucl. Fusion **64**, 086067 (2024).
[12] M. Wappl, S. A. Bozhenkov, T. Andreeva, S. Bannmann, H. M. Smith, R. C. Wolf (The W7-X Team), Plasma Phys. Controlled Fusion **67**, 075025 (2025).
[13] S. Bannmann, O. Ford, P. Poloskei, J. Svensson, A. Pavone, S. Kwak, U. Hoefel, E. Pasch, G. Fuchert, H. Smith, S. Lazerson, P. McNeely, N. Rust, D. Hartmann, R. Wolf (The W7-X Team), Nucl. Fusion **64**, 106015 (2024).
[14] T. Romba, F. Reimold, R. Jaspers, O. Ford, L. Vanó, T. Klinger (The W7-X Team), Nucl. Fusion **63**, 076023 (2023).
[15] T. Romba, F. Reimold, S. Bannmann, T. Bleher, O. P. Ford, P. Z. Poloskei, M. Wappl (The W7-X Team), Plasma Phys. Controlled Fusion **67**, 065016 (2025).
[16] N. T. Gladd, J. F. Drake, C. L. Chang, and C. S. Liu, Phys. Fluids **23**, 1182 (1980).
[17] J. F. Drake, N. T. Gladd, C. S. Liu, and C. L. Chang, Phys. Rev. Lett. **44**, 994 (1980).
[18] J. F. Drake and Y. C. Lee, Phys. Fluids **20**, 1341 (1977).
[19] A. Zocco, N. F. Loureiro, D. Dickinson, R. Numata, and C. M. Roach, Plasma Phys. Controlled Fusion **57**, 065008 (2015).
[20] W. Guttenfelder, J. Candy, S. M. Kaye, W. M. Nevins, E. Wang, R. E. Bell, G. W. Hammett, B. P. LeBlanc, D. R. Mikkelsen, and H. Yuh, Phys. Rev. Lett. **106**, 155004 (2011).
[21] X. Jian, C. Holland, J. Candy, E. Belli, V. Chan, A. M. Garofalo, and S. Ding, Phys. Rev. Lett. **123**, 225002 (2019).
[22] D. Hatch, M. Kotschenreuther, S. Mahajan, M. Pueschel, C. Michoski, G. Merlo, E. Hassan, A. Field, L. Frassinetti, C. Giroud, J. Hillesheim, C. Maggi, C. Perez von Thun, C. Roach, S. Saarelma, D. Jarema, F. Jenko, and J. Contributors, Nucl. Fusion **61**, 036015 (2021).
[23] F. Jenko, W. Dorland, M. Kotschenreuther, and B. N. Rogers, Phys. Plasmas **7**, 1904 (2000).
[24] H. Yamada, J. Harris, A. Dinklage, E. Ascasibar, F. Sano, S. Okamura, J. Talmadge, U. Stroth, A. Kus, S. Murakami, M. Yokoyama, C. Beidler, V. Tribaldos, K. Watanabe, and Y. Suzuki, Nucl. Fusion **45**, 1684 (2005).
[25] M. Beurskens *et al.* (The W7-X Team), Nucl. Fusion **61**, 116072 (2021).
[26] F. Merz, Gyrokinetic simulation of multimode plasma turbulence, Ph.D. thesis, Westfälischen Wilhelms-Universität Münster, 2009.
[27] M. Li, B. N. Breizman, and L. Zheng, J. Comput. Phys. **326**, 334 (2016).
[28] M. A. Beer, S. C. Cowley, and G. W. Hammett, Phys. Plasmas **2**, 2687 (1995).
[29] M. F. Martin, M. Landreman, P. Xanthopoulos, N. R. Mandell, and W. Dorland, Plasma Phys. Controlled Fusion **60**, 095008 (2018).
[30] P. Manas, Y. Camenen, S. Benkadda, W. A. Hornsby, and A. G. Peeters, Phys. Plasmas **22**, 062302 (2015).
[31] G. G. Plunk, J. W. Connor, and P. Helander, J. Plasma Phys. **83**, 715830404 (2017).
[32] J. H. E. Proll, P. Xanthopoulos, and P. Helander, Phys. Plasmas **20**, 122506 (2013).
[33] W. Guttenfelder, J. Candy, S. M. Kaye, W. M. Nevins, R. E. Bell, G. W. Hammett, B. P. LeBlanc, and H. Yuh, Phys. Plasmas **19**, 022506 (2012).
[34] X. Jian, C. Holland, J. Candy, S. Ding, E. Belli, V. Chan, G. M. Staebler, A. M. Garofalo, J. Mcclenaghan, and P. Snyder, Phys. Plasmas **28**, 042501 (2021).

[35] J. H. E. Proll, P. Helander, J. W. Connor, and G. G. Plunk, Phys. Rev. Lett. **108**, 245002 (2012).
[36] D. Carralero, T. Estrada, E. Maragkoudakis, T. Windisch, J. Alonso, M. Beurskens, S. Bozhenkov, I. Calvo, H. Damm, O. Ford, G. Fuchert, J. García-Regaña, N. Pablant, E. Sánchez, E. Pasch, J. Velasco (The W7-X Team), Nucl. Fusion **61**, 096015 (2021).
[37] F. Jenko and B. D. Scott, Phys. Plasmas **6**, 2418 (1999).
[38] M. Kotschenreuther, X. Liu, D. Hatch, S. Mahajan, L. Zheng, A. Diallo, R. Groebner, the DIII-D TEAM, J. Hillesheim, C. Maggi, C. Giroud, F. Koechl, V. Parail, S. Saarelma, E. Solano, A. Chankin, and J. Contributors, Nucl. Fusion **59**, 096001 (2019).
[39] H. Doerk, F. Jenko, M. J. Pueschel, and D. R. Hatch, Phys. Rev. Lett. **106**, 155003 (2011).
[40] P. Xanthopoulos, S. A. Bozhenkov, M. N. Beurskens, H. M. Smith, G. G. Plunk, P. Helander, C. D. Beidler, J. A. Alcusón, A. Alonso, A. Dinklage, O. Ford, G. Fuchert, J. Geiger, J. H. E. Proll, M. J. Pueschel, Y. Turkin, F. Warmer (The W7-X Team), Phys. Rev. Lett. **125**, 075001 (2020).
[41] P. Costello, J. Proll, G. Plunk, M. Pueschel, and J. Alcusón, J. Plasma Phys. **89**, 905890402 (2023).
[42] J. Proll, G. Plunk, B. Faber, T. Görler, P. Helander, I. McKinney, M. Pueschel, H. Smith, and P. Xanthopoulos, J. Plasma Phys. **88**, 905880112 (2022).
[43] L. Podavini, A. Zocco, J. García-Regaña, M. Barnes, F. Parra, A. Mishchenko, and P. Helander, J. Plasma Phys. **90**, 905900414 (2024).
[44] H. Thienpondt, J. García-Regaña, I. Calvo, G. Acton, and M. Barnes, Nucl. Fusion **65**, 016062 (2025).
[45] M. C. L. Morren, J. H. E. Proll, J. van Dijk, and M. J. Pueschel, Phys. Plasmas **31**, 052508 (2024).
[46] J. Duff, B. Faber, C. Hegna, M. Pueschel, and P. Terry, Nucl. Fusion **65**, 046020 (2025).
[47] J. D. Huba and S. P. Gary, Phys. Fluids **25**, 1821 (1982).
[48] D. E. Hastings and J. E. McCune, Phys. Fluids **25**, 509 (1982).
[49] A. Zocco, L. Podavini, F. Wilms, A. Bañón Navarro, and F. Jenko, Phys. Rev. Res. **6**, 033099 (2024).
[50] J. Lion *et al.*, Fusion Eng. Des. **214**, 114868 (2025).
[51] C. Hegna, D. Anderson, E. Andrew, A. Ayilaran, A. Bader, T. Bohm, K. C. Mata, J. Canik, L. Carbajal, A. Cerfon *et al.*, J. Plasma Phys. **91**, E76 (2025).
[52] L. Baylor, A. Geraud, W. Houlberg, D. Frigione, M. Gadeberg, T. Jernigan, J. D. Kloe, P. Kupschus, B. Kuteev, P. Lang, A. Oomens, A. Qualls, K. Sato, and G. Schmidt, Nucl. Fusion **37**, 445 (1997).